

Propagating and evanescent internal waves in a deep ocean model

M. S. PAOLETTI AND HARRY L. SWINNEY[†]

Department of Physics and Center for Nonlinear Dynamics, University of Texas at Austin,
Austin, TX, 78712, USA

(Received ?; revised ?; accepted ?. - To be entered by editorial office)

We present experimental and computational studies of the propagation of internal waves in a stratified fluid with an exponential density profile that models the deep ocean. The buoyancy frequency profile $N(z)$ (proportional to the square root of the density gradient) smoothly varies by nearly an order of magnitude over the fluid depth, rather than being constant or piecewise-constant as in prior studies. In addition to being nonuniform, the stratification is characterized by a turning depth z_c , where $N(z_c)$ is equal to the wave frequency ω and $N(z < z_c) < \omega$. Internal waves reflect from the turning depth and become evanescent below. The energy flux below the turning depth is shown to decay exponentially with a decay constant given by k_c , which is the horizontal wavenumber at the turning depth. The vertical velocity fields of the incoming and reflected waves above the turning depth agree within a few percent with a previously untested theory for a fluid of arbitrary stratification [Kistovich and Chashechkin, *J. App. Mech. Tech. Phys.* **39**, 729-737 (1998)].

Key words: Authors should not enter keywords

1. Introduction

In a stratified fluid, an internal wave transports momentum and energy as the propagating disturbance is restored by buoyancy forces. In the absence of rotation, internal waves satisfy the following dispersion relation

$$\frac{\omega}{N(z)} = \sin(\theta(z)), \quad (1.1)$$

where ω is the angular frequency of the wave, θ is the angle of propagation relative to the horizontal, $N(z) = \sqrt{-(g/\rho_0)(d\rho/dz)}$ is the buoyancy frequency, g is the gravitational acceleration, ρ_0 is a reference density and $\rho(z)$ is the density profile. Approximately half of the internal wave energy in the ocean is produced by tidal flow over bottom topography (Munk & Wunsch 1998; Wunsch & Ferrari 2004), resulting in waves at the lunar semidiurnal tidal frequency $\omega_{M2} = 1.0452 \times 10^{-4}$ rad/s, called internal tides.

Oceanic buoyancy frequencies vary greatly, decreasing from the values in the thermocline to become two orders of magnitude smaller in the abyss where the water is well mixed. Pingree & New (1991) found that deep in the Bay of Biscay the value of $N(z)$ became so small that the internal waves became nearly vertical (Eq. 1.1) at the point of reflection from the bottom topography. Recently King *et al.* (2012) analyzed data for pressure, temperature, and salinity for thousands of locations throughout the oceans and

[†] Email address for correspondence: swinney@chaos.utexas.edu

found that in many locations in the deep oceans the buoyancy frequency becomes even smaller than ω_{M2} . Internal waves approaching a *turning depth* z_c where $N(z_c) = \omega_{M2}$ become vertical by (1.1) and then reflect from the turning surface; below the turning depth the waves are evanescent (exponentially damped).

Recent studies have examined internal waves in piecewise-linear stratifications (Sutherland & Yewchuk 2004; Mathur & Peacock 2009, 2010; Gregory & Sutherland 2010). Building on that work, we examine internal wave propagation in stratified fluids with continuously varying $N(z)$, as in the ocean. This physically important case was considered by Kistovich & Chashechkin (1998), who developed a linear theory that describes the propagation of internal waves in arbitrary stratifications, including those that contain a turning depth.

We have conducted laboratory experiments and direct numerical simulations for a stratified fluid with $N(z)$ designed to mimic ocean conditions, including a turning depth. Our laboratory and numerical results are found to agree well, and our results for reflected and evanescent waves agree within a few percent with the theoretical predictions of Kistovich and Chashechkin.

The rest of the paper is organized as follows. In §2 we summarize the results of the theory of Kistovich & Chashechkin (1998) for wave reflection from a turning depth. In §3 we describe our numerical and experimental methods. In §4 we present our results, the consequences of which are discussed in §5.

2. Kistovich-Chashechkin theory

The theory of Kistovich & Chashechkin (1998) describes the propagation of internal wave beams in arbitrary stratifications. The theory accounts for the role of viscous dissipation, diffusion and the interaction of an internal wave beam with a turning depth. The density profile is assumed to be $\rho_0(z) = \rho_{00} [1 + s_0(z)]$, where s_0 is the reduced salinity and ρ_{00} is a reference density. The internal wavefield is assumed to be two-dimensional and to have a time-dependence of the form $\exp(-i\omega t)$ (which is henceforth omitted). Then the linear Navier-Stokes equations in the Boussinesq approximation become

$$-i\omega u = -\frac{1}{\rho_{00}} \frac{\partial p}{\partial x} + \nu \Delta u, \quad -i\omega w = -\frac{1}{\rho_{00}} \frac{\partial p}{\partial z} + \nu \Delta w - sg \quad (2.1)$$

$$-i\omega s + w \frac{ds_0}{dz} = D \Delta s, \quad \frac{\partial u}{\partial x} + \frac{\partial w}{\partial z} = 0, \quad (2.2)$$

where u is the horizontal velocity, w the vertical velocity, p and s the variable pressure and salinity, ν the kinematic viscosity, D the salt diffusivity, g gravitational acceleration (in the direction $-\hat{z}$), and $\Delta = \partial^2/\partial x^2 + \partial^2/\partial z^2$ is the two-dimensional Laplacian.

The internal wavefield may be described by the vertical displacement $h(x, z)$, which is related to the vertical velocity by $w = -i\omega h$. Solutions may be sought in the form

$$h(x, z) = \int_0^\infty f(z, k) \exp(ikx) dk, \quad (2.3)$$

where k is the wavenumber.

Asymptotic solutions for f may be obtained if $N(z)$ varies slowly compared to the length scales describing the internal wave beam. Given their assumptions, Kistovich and Chashechkin obtain

$$f(z, k) = \frac{A(k)}{\sqrt{\gamma}} \exp \left[\frac{i\tilde{\nu}k^2 (1 - 3\gamma^4)}{4\omega\gamma^2} \right] \exp \left\{ i\xi k \int_{z_0}^z \left[\gamma - \frac{i\tilde{\nu}k^2 (1 + \gamma^2)^2}{2\omega\gamma} \right] dz' \right\}, \quad (2.4)$$

where $A(k)$ describes the spectral properties of the wave source located at (x_0, z_0) , $\tilde{\nu} =$

$\nu + D$, $\xi = 1$ (-1) corresponds to beams propagating down (up) and to the right, and

$$\gamma^2(z) = \frac{N^2(z) - \omega^2}{\omega^2}. \quad (2.5)$$

Thus, given $A(k)$ and $N(z)$, the theory of Kistovich and Chashechkin predicts the vertical velocity field everywhere in space.

In addition to examining the propagation of internal wave beams in arbitrary stratifications, Kistovich and Chashechkin derived the following expressions for the reflection of an internal wave beam from a turning depth z_c , defined as $N(z_c) = \omega$ and $N(z) < \omega$ for all $z < z_c$:

$$f_i(z, k) = \frac{A(k)}{\sqrt{|\gamma|}} \exp \left[\frac{i\tilde{\nu}k^2(1-3\gamma^4)}{4\omega\gamma^2} + ik \int_{z_0}^z \left\{ \gamma - \frac{i\tilde{\nu}k^2(1+\gamma^2)^2}{2\omega\gamma} \right\} dz' \right], \quad (2.6)$$

$$f_r(z, k) = \frac{B(k)}{\sqrt{|\gamma|}} \exp \left[\frac{i\tilde{\nu}k^2(1-3\gamma^4)}{4\omega\gamma^2} - ik \int_{z_c}^z \left\{ \gamma - \frac{i\tilde{\nu}k^2(1+\gamma^2)^2}{2\omega\gamma} \right\} dz' \right], \quad (2.7)$$

$$f_t(z, k) = \frac{C(k)}{\sqrt{|\gamma|}} \exp \left[\frac{i\tilde{\nu}k^2(1-3\gamma^4)}{4\omega\gamma^2} + k \int_{z_c}^z \left\{ |\gamma| + \frac{i\tilde{\nu}k^2(1+\gamma^2)^2}{2\omega|\gamma|} \right\} dz' \right], \quad (2.8)$$

where f_i describes the incoming wave beam for $x < x_c$ and $z > z_c$, f_r is the reflected wave for $x > x_c$ and $z > z_c$ and f_t is the transmitted (evanescent) wave for $z < z_c$. Given the spectral amplitudes $A(k)$, we have

$$B(k) = A(k)e^{-i\phi_0}e^{i\pi/2}, \quad C(k) = A(k)e^{-i\phi_0}e^{i\pi/4}, \quad (2.9)$$

where

$$\phi_0 = k \int_{z_0}^{z_c} \left[\gamma - \frac{i\tilde{\nu}k^2(1+\gamma^2)^2}{2\omega\gamma} \right] dz', \quad (2.10)$$

which takes into account the phase winding and viscous decay as the beam propagates from the source at (x_0, z_0) to the turning depth at (x_c, z_c) . Therefore, only $N(z)$ and $A(k)$ are required to fully characterize the vertical velocity field.

3. Methods

3.1. Direct Numerical Simulations

We numerically simulate internal wave propagation in nonlinear stratifications using CDP 2.4, which is a large eddy simulation code developed by Ham & Iaccarino (2004). By disabling all subgrid-scale modeling, we perform direct numerical simulations of the incompressible Navier-Stokes equation. The code is a parallel, unstructured finite-volume-based solver that is modeled after the algorithm presented by Mahesh *et al.* (2004). Second-order accuracy in space and time is achieved by using a fractional step time marching scheme and multiple implicit schemes for the spatial operators (Ham *et al.* 2006). We perform two-dimensional simulations in the Boussinesq approximation. These approximations are justified by the small density variation and predominantly two-dimensional flows examined in the experiments. CDP solves the following equations for the pressure p , density ρ and velocity $\mathbf{v} = (u, w)$ in the (x, z) directions:

$$\partial \mathbf{v} / \partial t + (\mathbf{v} \cdot \nabla) \mathbf{v} = -\nabla p / \rho_0 - g\rho / \rho_0 \hat{\mathbf{z}} + \nu \nabla^2 \mathbf{v} + \mathbf{F} / \rho_0, \quad (3.1)$$

$$\nabla \cdot \mathbf{v} = 0, \quad \partial \rho / \partial t + (\mathbf{v} \cdot \nabla) \rho = D \nabla^2 \rho, \quad (3.2)$$

where $\rho_0 = 1000 \text{ kg/m}^3$ is a reference density, g is the gravitational acceleration, ν is the kinematic viscosity, \mathbf{F} drives the internal waves, as described below, and $D = 10^{-12} \text{ m}^2/\text{s}$ is the density diffusion coefficient. The value of D is so small that salt diffusion in the simulations is negligible; this is an accurate representation of the experiments.

Internal waves are generated by the forcing term \mathbf{F} shown in Eq. (3.1), which is similar to that used by Slinn & Riley (1998), Javam *et al.* (1999) and Rodenborn *et al.* (2011):

$$\mathbf{F}(x, z) = (\nabla \times \nabla \times \Phi \hat{z}) \sin(\omega t), \quad (3.3)$$

$$\Phi(x, z) = \Phi_0 \exp \left[- \left(a(x - x_0)^2 + 2b(x - x_0)(z - z_0) + c(z - z_0)^2 \right) \right], \quad (3.4)$$

where $a = \cos^2(\beta)/2\sigma_x^2 + \sin^2(\beta)/2\sigma_z^2$, $b = \sin(2\beta)/4\sigma_x^2 - \sin(2\beta)/4\sigma_z^2$, $c = \sin^2(\beta)/2\sigma_x^2 + \cos^2(\beta)/2\sigma_z^2$, ω is the internal wave frequency, Φ_0 the maximum forcing amplitude, (x_0, z_0) the spatial center, β the counterclockwise rotation of the elliptical Gaussian forcing profile, and σ_x (σ_z) is the horizontal (vertical) standard deviation. The angle β is chosen so that the forcing profile is aligned with the local internal wave propagation angle θ . The oscillation frequency is $\omega_0 = 0.628 \text{ rad/s}$ for all of the simulations and experiments except for Run 12 where $\omega = \omega_0/4$ (see table 1). The time step is $\Delta t = \pi/4000\omega$, which yields 8000 time steps per period. We run the simulations for 40 periods to ensure that the system has reached a steady-state. The forcing amplitude Φ_0 and standard deviations σ_x and σ_z are varied to modify the properties of the wave beam, as described in table 1.

Two computational grids are generated using Pointwise Gridgen. Grid I is designed for direct comparison of the numerical simulations with the experiments. The domain has the same dimensions as the experimental tank, namely $0 < x < 0.9 \text{ m}$ and $0 < z < 0.6 \text{ m}$. The numerical wavemaker is centered at $(x_0 = 0.15 \text{ m}, z_0 = 0.50 \text{ m})$ in both the simulations and experiments. While the grid is structured everywhere (composed of rectangular control volumes), the horizontal and vertical resolutions vary smoothly throughout the domain to take into account the variable shear as the beam propagates in the nonlinear stratification. Near the wavemaker the wave beam is nearly horizontal, resulting in strong vertical shear, while at the turning depth the beam propagates vertically, necessitating increased horizontal resolution. At the wavemaker center we use a horizontal resolution of $\Delta x = 2.5 \text{ mm}$, while the vertical resolution is $\Delta z = 0.4 \text{ mm}$. The resolutions near the reflection from the turning depth at (x_c, z_c) are $\Delta x = 0.4 \text{ mm}$ and $\Delta z = 1.5 \text{ mm}$. Grid I is composed of approximately 5.5×10^5 control volumes. No-slip boundary conditions are enforced at $x = 0$, $z = 0$, and $x = 0.90 \text{ m}$. The top surface at $z = 0.60 \text{ m}$ is a free-slip, impenetrable boundary chosen to emulate the free surface in the experiments. The internal waves are damped for $x > 0.8 \text{ m}$ by adding a drag force equal to $-0.002\mathbf{v}$ to Eq. (3.1) to mimic the absorbent material present in the experiments.

Grid II is designed to compare the numerical simulations with the theoretical predictions of Kistovich & Chashechkin (1998), which are described in §2. The grid spans $0 < x < 6 \text{ m}$ and $0 < z < 2 \text{ m}$. The wavemaker is centered at $(x_0 = 1.0 \text{ m}, z_0 = 1.5 \text{ m})$. As with Grid I, the spatial resolution varies smoothly throughout the domain to account for the variation in the beam angle as it propagates. The horizontal resolution in the vicinity of the wavemaker is $\Delta x = 15 \text{ mm}$ while the vertical resolution is $\Delta z = 2 \text{ mm}$. Near the reflection at the turning depth the horizontal resolution is $\Delta x = 4 \text{ mm}$ and the vertical resolution is $\Delta z = 6 \text{ mm}$. Grid II has a total of $\sim 2.5 \times 10^5$ control volumes. No-slip boundary conditions are applied at all of the boundaries. To reduce finite-size effects, a drag force of the form $-0.02\mathbf{v}$ is added to Eq. 3.1 for $x < 0.6 \text{ m}$, $x > 5.5 \text{ m}$ and $z > 1.75 \text{ m}$ to damp the wave beams before they reach the boundaries.

The density profiles are chosen to be scaled models of the stratification in the deep ocean. In particular, we are interested in examining the dynamics of internal waves at

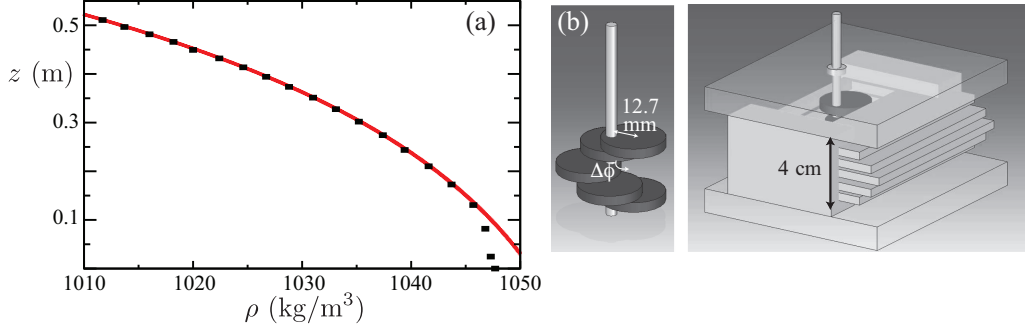


FIGURE 1. (a) The experimental density profile (black squares) agrees well in the domain of interest with the density profile given by Eq. (3.5) and used in the simulations (red line). (b) The experimental wave maker consists of five acrylic plates in a box (right) that are driven by a rotating camshaft (left). Each successive cam is rotated by 45° , which results in a half-sine wave configuration.

turning depths analogous to those recently discovered by King *et al.* (2012). As such, all of our density profiles are exponentials with a turning depth at z_c , where $N(z) < \omega$ for $z < z_c$. However, the results presented here do not depend upon the stratification being exponential in form; the crucial aspect is the existence of a turning depth. The stratification used for the experimental domain covered by Grid I is shown as the red line in Fig. 1, and is given by

$$\rho_{\text{expt}} = 1061 - 10 \exp(3.12z) \text{ kg/m}^3, \quad 0 \leq z \leq 0.6 \text{ m}. \quad (3.5)$$

The depth-dependent buoyancy frequency $N_{\text{expt}}(z)$ has a turning depth at $z_c = 0.082 \text{ m}$. The density profile used for all simulations with Grid II, except Run 12, is given by

$$\rho_{\text{sim}} = \begin{cases} 1244 - 5.75 \exp(2.5z), & 0 \leq z \leq 1.5 \text{ m} \\ 1916 - 611z, & 1.5 < z \leq 2 \text{ m}. \end{cases} \quad (3.6)$$

The resulting buoyancy frequency profile varies by a factor of 6.5 from top to bottom and has a turning depth at $z_c = 0.424 \text{ m}$. The density profile for Run 12 has $N(z)$ reduced by a factor of 4 for all depths.

3.2. Experimental Methods

Experiments are performed in a glass tank with $0 < x < 0.90 \text{ m}$, $0 < y < 0.45 \text{ m}$ and $0 < z < 0.60 \text{ m}$. The exponential gradient given by Eq. (3.5) is generated by utilizing the generalized version of the double-bucket method (Fortuin 1960; Oster 1965) described by Hill (2002). The density profile is measured by extracting fluid samples at known heights, which are then measured with an Anton Paar density meter. An example experimental stratification is shown as the black squares in Fig. 1(a). The fluid at the top ($z = 0.59 \text{ m}$) has $\rho = 1000 \text{ kg/m}^3$. The experimental density profile agrees well with the stratification used in the simulations (red line and Eq. (3.5)) for $0.1 < z < 0.5 \text{ m}$.

Internal wave beams are generated using a wave maker similar to the one developed by Gostiaux *et al.* (2007). Our wave maker (Rodenborn *et al.* 2011) consists of five acrylic plates with dimensions $150 \text{ mm} \times 150 \text{ mm} \times 6 \text{ mm}$ that are separated by 2.5 mm and placed within a parallelepiped open-sided box, as shown in Fig. 1(b). A helicoidal rotating camshaft oscillates the plates periodically with the direction of rotation setting the internal wave phase velocity vector. The eccentricity of the camshaft (12.7 mm) determines the oscillation amplitude. The generated wave beams are nearly two-dimensional, particularly along the center of the tank ($y = 0.225 \text{ m}$) where all of our measurements

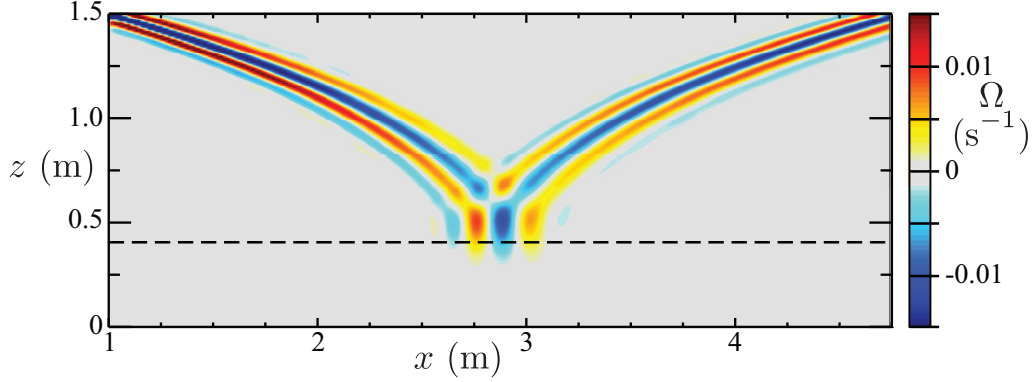


FIGURE 2. Snapshot of the vorticity (color) for a wave beam generated in the simulations at $(x = 1 \text{ m}, z = 1.5 \text{ m})$ after 40 periods of oscillation. The stratification (Eq. (3.6)) has a turning depth at $z_c = 0.424 \text{ m}$ (dashed line).

are taken. The wave maker is centered at $(x_0 = 0.15 \text{ m}, z_0 = 0.50 \text{ m})$ and oriented such that the plates are parallel to the wave beam angle at $z = z_0$. The internal wave motions are dissipated by a fiber mesh for $x > 0.88 \text{ m}$ to reduce finite-size effects.

Particle image velocimetry (Adrian 1991) is used to obtain the two-dimensional velocity field $\mathbf{v} = (u, w)$ in the vertical plane given by $y = 0.225 \text{ m}$. Hollow glass spheres with diameters $8 < d < 12 \mu\text{m}$ and densities in the range $1050 < \rho < 1150 \text{ kg/m}^3$ are used as seed particles. The tracers are illuminated by a 5 mm thick laser sheet produced by a 532 nm wavelength laser (2.5 W). Two 12-bit CCD cameras with 1296×966 pixel resolution capture orthogonally scattered light in a $194 \times 145 \text{ mm}^2$ region, 40 times per period ($\Delta t = 0.25 \text{ s}$). The instantaneous velocity fields are determined using the CIV algorithm developed by Fincham & Delerce (2000) and are interpolated to a regular 50×50 grid with spatial resolutions of $\Delta x = 3.9 \text{ mm}$ and $\Delta z = 2.9 \text{ mm}$.

4. Results

An example snapshot of a wave beam propagating in the stratification given by Eq. (3.6) is shown in Fig. 2 (see movies in online supplementary material), with vorticity $\Omega = \nabla \times \mathbf{v}$ indicated by color and the turning depth $z = z_c$ given by the dashed line. As can be seen, the beam generated at $(x = 1.0 \text{ m}, z = 1.5 \text{ m})$ propagates down and to the right before being reflected at the turning depth, causing the energy to move up and to the right. Only a small fraction of the energy flux penetrates below the turning depth.

We compare the velocity and vorticity fields of the numerical simulations with the experimental measurements to verify the computations, as illustrated by the incoming and reflected beam profiles in Fig. 3. Horizontal profiles of the vertical velocity are well described by modulated Gaussians of the form

$$w(x, z, t) = A_0(z) \cos(k_0(z)x - \omega t) \exp\left(-[x - \mu(z)]^2 / 2\sigma(z)^2\right) [\gamma(z_0)/\gamma(z)]^{1/2}, \quad (4.1)$$

where A_0 is the velocity amplitude, k_0 the wavenumber, μ the beam center, σ the beam width, and the term $[\gamma(z_0)/\gamma(z)]^{1/2}$ accounts for the increase (decrease) in the vertical velocity as the beam propagates into weaker (stronger) stratification. Therefore, even though the vertical velocity may increase by geometrical effects as a beam propagates into weaker stratifications, the velocity amplitude A_0 monotonically decreases owing to

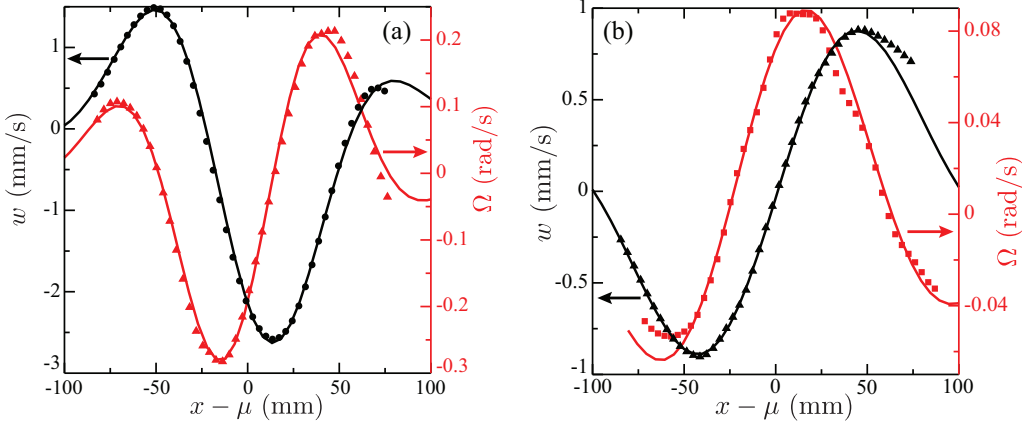


FIGURE 3. Snapshots of the vertical velocity (black) and vorticity (red) horizontal cross-sections centered at (a) ($\mu = 0.30$ m, $z = 0.40$ m) for the incoming wave beam and (b) ($\mu = 0.76$ m, $z = 0.37$ m) for the reflected wave beam. Laboratory measurements are given by the data points and results from the simulations are shown as solid lines.

viscous dissipation. We find that the experimental and computational vertical velocity and vorticity profiles are in remarkable agreement, as Fig. 3 illustrates.

4.1. Evanescent internal waves

Below the turning depth z_c , internal waves become evanescent with an intensity that decays exponentially with a decay constant α (Gostiaux *et al.* 2006). We compute the intensity of the evanescent wave beams by horizontally integrating the vertical flux at different depths,

$$\Phi(z) = \int p' w' dx, \quad (4.2)$$

where p' and w' are the fluctuations in the pressure and vertical velocity, respectively. Figure 4(a) shows example results for the vertical flux below the turning depth. The distance from the turning depth $z_c - z$ is scaled by the horizontal wavenumber at the turning depth $k_c \equiv k_0(z_c)$, which is given near each curve. Below the turning depth, the flux decays exponentially, except for large $z_c - z$ where bottom-boundary interactions arrest the decay.

Our measurements of the decay constants α agree well with the expected values $\alpha = k_c$ (see Fig. 4(b) and the summary in table 2). Therefore, in analogy with evanescence in other contexts, we conclude that the flux is well described by

$$\Phi(z) = \Phi(z_c) e^{-k_c(z_c - z)}, \quad \text{for } z < z_c. \quad (4.3)$$

4.2. Internal wave reflection: comparison with theory

The theory of Kistovich & Chashechkin (1998) described in §2 provides predictions with *no free parameters* for the behavior of the vertical velocity field of internal waves propagating in nonlinear stratifications, even those with a turning depth. To test these predictions, we compare horizontal cross-sections of the vertical velocity field computed by our numerical simulations to the theoretical predictions. Beam profiles are fit to the form (4.1) to determine the amplitude $A_0(z)$, wavenumber $k_0(z)$, beam center $\mu(z)$ and beam width $\sigma(z)$, as the beam propagates towards the turning depth, reflects, and then propagates away.

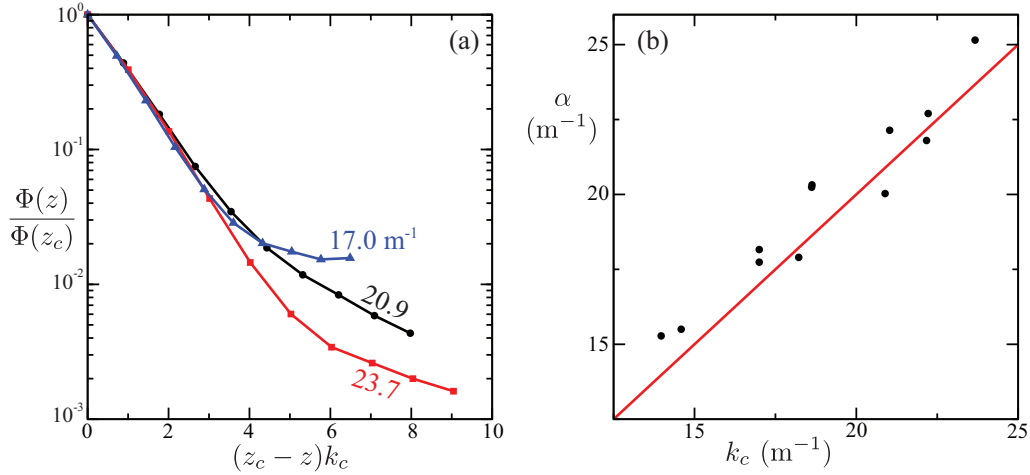


FIGURE 4. (a) Results from the numerical simulations for the horizontally integrated flux $\Phi(z)$, defined by Eq. (3.4), for evanescent waves beneath the turning depth z_c . The horizontal wavenumber at the turning depth, k_c , is indicated next to the corresponding curve. (b) The decay constant α from simulations (black circles) is compared to the horizontal wavenumber at the turning depth, k_c (red line).

To use the theoretical expressions Eqs. (2.6) and (2.7) for the incoming and reflected wave beams, we must know the stratification $N(z)$ and the spectral amplitudes of the wave source $A(k)$. The buoyancy frequency profile may be determined using Eq. (3.6). We determine $A(k)$ by fitting a horizontal cross-section of the vertical velocity near the wave source to Eq. (4.1), which we then Fourier transform analytically to determine the spectral amplitudes. We then compute the predicted vertical velocity field for the incoming and reflected wave beams using Eqs. (2.6) and (2.7).

The numerical simulations and theoretical predictions are compared by measuring the velocity amplitude $A_0(z)$, using the same values of $\{k_0(z), \mu(z), \text{ and } \sigma(z)\}$ for the simulations and theory. The simulation results for $A_0(z)$ as a function of the geometric length from the turning depth $(L - L_c)$ are compared to theory in Fig. 5, where

$$L(z) = \int_{z_0}^z \sqrt{1 + \gamma^2(z')} dz', \quad (4.4)$$

is the distance from the wave source measured along the centerline of the beam, and $L_c \equiv L(z_c)$. The four curves in Fig. 5(a) correspond to different viscosity values, as indicated. Figure 5(b) compares cases with the same viscosity but different values of the source wavenumber, source amplitude, or wave frequency, as indicated. In all cases that we have studied, the fully-constrained theoretical predictions agree (on average) within 1.5% of the numerical simulations, as summarized in table 2.

5. Discussion

We have presented laboratory experiments and direct numerical simulations of internal wave beams propagating in a fluid where the buoyancy frequency $N(z)$ decreases exponentially as the bottom boundary is approached, as is often found in the abyssal ocean. We have examined wave propagation in a fluid with a turning depth z_c , below which $N(z) < \omega$, as occurs at many locations in the ocean (King *et al.* 2012). The experiments and simulations agree within a few percent with the predictions of the previously

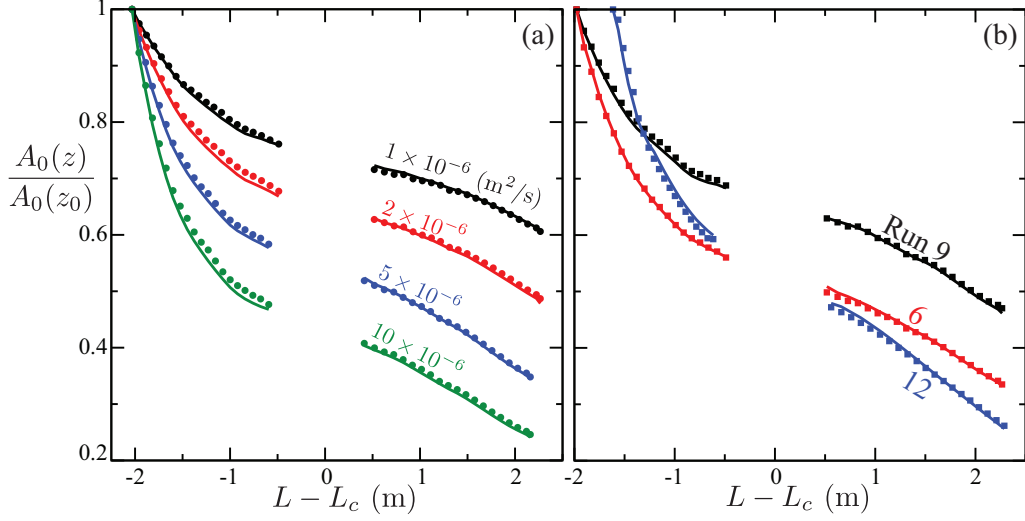


FIGURE 5. The vertical velocity amplitude $A_0(z)$ in the simulations (data points) is compared with the fully constrained theoretical predictions of Kistovich and Chashechkin (solid lines) (a) for varying viscosity values, and (b) for fixed viscosity ($5 \times 10^{-6} \text{ m}^2/\text{s}$) and other parameters given by $(\omega, k_0(z_0), \sigma(z_0))$: Run 6, (0.63 rad/s, 18.7 m^{-1} , 0.127 m); Run 9, (0.63 rad/s, 22.3 m^{-1} , 0.144 m); Run 12 (0.16 rad/s, 22.3 m^{-1} , 0.144 m).

untested linear theory of Kistovich & Chashechkin (1998) for internal wave beam propagation in a fluid with arbitrary stratification. Thus if the stratification $N(z)$ and the internal wave beam spectral amplitude $A(k)$ are known, the velocity field of a propagating internal wave beam can be predicted with no free parameters, as long as topography and nonlinear interactions are negligible.

The horizontally-integrated flux below a turning depth decays exponentially with a decay constant $\alpha = k_c$, where k_c is the horizontal wavenumber at the turning depth. This decay may greatly limit the role of internal tides beneath turning depths. For example, a wave beam with a wavelength $\lambda \sim 300 \text{ m}$ incident upon a turning depth will produce an evanescent beam with a horizontally-integrated flux that decays by an order of magnitude every $\sim 100 \text{ m}$ beneath the turning depth. King *et al.* (2012) found that in some locations turning depths occur at depths greater than 1 km above the ocean bottom.

Another consequence of the existence of locations with turning depths well above the ocean floor is the effect on internal wave generation by tidal flow over topography in a region where internal waves are evanescent. If the turning depth is near the ocean floor, the internal waves could tunnel through the fluid beneath the turning depth, but in general internal tides generated below a turning depth will be greatly reduced in intensity by the exponential damping. Thus future studies should examine the effect of turning depths on internal tide generation for a wide range of parameters (e.g., turning depth height, $N(z)$, tidal frequency).

6. Acknowledgments

We thank Bruce Rodenborn and Phillip Morrison for insightful discussions. This research was supported by the Office of Naval Research MURI Grant N000141110701.

REFERENCES

- ADRIAN, R. J. 1991 Particle-imaging techniques for experimental fluid-mechanics. *Ann. Rev. Fluid Mech.* **23**, 261–304.
- FINCHAM, A. & DELERCE, G. 2000 Advanced optimization of correlation imaging velocimetry algorithms. *Exp. Fluids* **29**, 13–22.
- FORTUIN, J. M. H. 1960 Theory and application of two supplementary methods of constructing density gradient columns. *J. Polymer Sci.* **44**, 505–515.
- GOSTIAUX, L., DAUXOIS, T., DIDELLE, H., SOMMERIA, J. & VIBOUD, S. 2006 Quantitative laboratory observations of internal wave reflection on ascending slopes. *Phys. Fluids* **18**, 056602.
- GOSTIAUX, L., DIDELLE, H., MERCIER, S. & DAUXOIS, T. 2007 A novel internal waves generator. *Exp. Fluids* **42**, 123–130.
- GREGORY, K. D. & SUTHERLAND, B. R. 2010 Transmission and reflection of internal wave beams. *Phys. Fluids* **22**, 106601.
- HAM, F. & IACCARINO, G. 2004 Energy conservation in collocated discretization schemes on unstructured meshes. In *Annual Research Briefs (Center for Turbulence Research, Stanford, CA)*, pp. 3–14.
- HAM, F., MATSSON, K. & IACCARINO, G. 2006 Accurate and stable finite volume operators for unstructured flow solvers. In *Annual Research Briefs (Center for Turbulence Research, Stanford, CA)*, pp. 243–261.
- HILL, D. F. 2002 General density gradients in general domains: the “two-tank” method revisited. *Exp. Fluids* **32**, 434–440.
- JAVAM, A., IMBERGER, J. & ARMFIELD, S. W. 1999 Numerical study of internal wave reflection from sloping boundaries. *J. Fluid Mech.* **396**, 183–201.
- KING, B., STONE, M., ZHANG, H. P., GERKEMA, T., MARDER, M., SCOTT, R. B. & SWINNEY, H. L. 2012 Buoyancy frequency profiles and internal semidiurnal tide turning depths in the oceans. *J. Geophys. Res. - Oceans*, in press.
- KISTOVICH, YU. V. & CHASHECHKIN, YU. D. 1998 Linear theory of the propagation of internal wave beams in an arbitrarily stratified liquid. *J. App. Mech. Tech. Phys.* **39**, 729–737.
- MAHESH, K., CONSTANTINESCU, G. & MOIN, P. 2004 A numerical method for large-eddy simulation in complex geometries. *J. Comput. Phys.* **197**, 215–240.
- MATHUR, M. & PEACOCK, T. 2009 Internal wave beam propagation in non-uniform stratifications. *J. Fluid Mech.* **639**, 133–152.
- MATHUR, M. & PEACOCK, T. 2010 Internal wave interferometry. *Phys. Rev. Lett.* **104**, 118501.
- MUNK, W. & WUNSCH, C. 1998 Abyssal recipes II: energetics of tidal and wind mixing. *Deep-Sea Research Part I-Oceanographic Research Papers* **45**, 1977–2010.
- OSTER, G. 1965 Density Gradients. *Sci. Am.* **213**, 70.
- PINGREE, R. D. & NEW, A. L. 1991 Abyssal penetration and bottom reflection of internal tidal energy in the Bay of Biscay. *J. Phys. Oceanography* **21**, 28–39.
- RODENBORN, B., KIEFER, D., ZHANG, H. P. & SWINNEY, H. L. 2011 Harmonic generation by reflecting internal waves. *Phys. Fluids* **23**, 026601.
- SLINN, D. N. & RILEY, J. J. 1998 A model for the simulation of turbulent boundary layers in an incompressible stratified flow. *J. Comput. Phys.* **144**, 550–602.
- SUTHERLAND, B. R. & YEWCHUK, K. 2004 Internal wave tunnelling. *J. Fluid Mech.* **511**, 125–134.
- WUNSCH, C. & FERRARI, R. 2004 Vertical mixing, energy and the general circulation of the oceans. *Ann. Rev. Fluid Mech.* **36**, 281–314.

| Run | ω (rad/s) | ν ($\times 10^{-6}$ m ² /s) | $A_0(z_0)$ (mm/s) | $k_0(z_0)$ (m ⁻¹) | $\sigma(z_0)$ (m) |
|-----|------------------|---|-------------------|-------------------------------|-------------------|
| 1 | 0.63 | 1 | 0.29 | 24.1 | 0.109 |
| 2 | 0.63 | 2 | 0.27 | 23.8 | 0.111 |
| 3 | 0.63 | 5 | 0.22 | 22.0 | 0.124 |
| 4 | 0.63 | 10 | 0.18 | 20.7 | 0.135 |
| 5 | 0.63 | 1 | 1.37 | 23.2 | 0.123 |
| 6 | 0.63 | 5 | 1.13 | 22.3 | 0.127 |
| 7 | 0.63 | 5 | 3.38 | 18.4 | 0.157 |
| 8 | 0.63 | 5 | 0.12 | 14.6 | 0.176 |
| 9 | 0.63 | 5 | 0.16 | 18.7 | 0.144 |
| 10 | 0.63 | 5 | 0.25 | 25.5 | 0.117 |
| 11 | 0.63 | 5 | 0.09 | 25.9 | 0.137 |
| 12 | 0.16 | 5 | 0.33 | 16.5 | 0.189 |

TABLE 1. Parameters describing the direct numerical simulations performed with Grid II and ρ_{sim} , used to compare to the theory of Kistovich & Chashechkin (1998). Horizontal cross-sections of the vertical velocity field near the wave source are given by $w(x, t) = A_0(z_0) \cos(k_0(z_0)x - \omega t) \exp[-(x - \mu(z_0))^2/2\sigma(z_0)]$, where A_0 is the velocity amplitude, ω the angular frequency, k_0 the wavenumber and σ the beam width. The kinematic viscosity ν is constant throughout the simulation domain.

| Run | $\Phi(z_c)$ (10^{-7} kg/s ³) | k_c (m ⁻¹) | α (m ⁻¹) | δ (%) |
|-----|---|--------------------------|-----------------------------|--------------|
| 1 | -3.82 | 22.2 | 22.7 | 0.48 |
| 2 | -4.15 | 21.0 | 22.1 | 1.08 |
| 3 | -3.63 | 18.6 | 20.3 | 0.96 |
| 4 | -2.52 | 17.0 | 18.2 | 2.08 |
| 5 | -107 | 22.2 | 21.8 | 2.28 |
| 6 | -92.6 | 18.6 | 20.2 | 0.50 |
| 7 | -1721 | 18.2 | 17.9 | 0.74 |
| 8 | -1.81 | 14.6 | 15.5 | 3.42 |
| 9 | -2.70 | 17.0 | 17.7 | 0.86 |
| 10 | -3.89 | 20.9 | 20.0 | 2.77 |
| 11 | -0.91 | 23.7 | 25.2 | 2.20 |
| 12 | -4.90 | 14.0 | 15.3 | 1.39 |

TABLE 2. Summary of results presented in Figs. 4 and 5, where $\Phi(z_c)$ is the horizontally-integrated vertical flux at the turning depth, k_c is the horizontal wavenumber at the turning depth, α is the decay constant describing the exponential decay of the vertical flux below the turning depth, and δ is the mean absolute percent difference between our measurements of $A_0(z)$ and the theoretical predictions of Kistovich & Chashechkin (1998).
